Hindawi
Journal of Engineering
Volume 2023, Article ID 8828300, 20 pages
https://doi.org/10.1155/2023/8828300

Research Article

Thermal Analysis on Kerosene Oil-Based Two Groups of Ternary Hybrid Nanoparticles (CNT-Gr-Fe_3O_4 and MgO-Cu-Au) Mix Flow over a Bidirectional Stretching Sheet: A Comparative Approach

Shilpa Choudhary,[1] Ruchika Mehta,[1] Nazek Alessa,[2] Sanju Jangid,[1] and M. Venkateswar Reddy[3]

[1]*Department of Mathematics & Statistics, Manipal University Jaipur, Jaipur, India*
[2]*Department of Mathematical Sciences, College of Sciences, Princess Nourah Bint Abdulrahman University, P.O. Box 84428, Riyadh 11671, Saudi Arabia*
[3]*Department of Mechanical Engineering, MLR Institute of Technology, Hyderabad, Telangana, India*

Correspondence should be addressed to Ruchika Mehta; ruchika.mehta@jaipur.manipal.edu and Nazek Alessa; nazekaa@yahoo.com

Received 4 July 2023; Revised 23 October 2023; Accepted 28 October 2023; Published 20 November 2023

Academic Editor: Samuel E. Sanni

The present work examines the impressions of radiation impact on the three-dimensional non-Newtonian MHD Casson flow of ternary hybrid nanofluids over a symmetrical stretching sheet with magnetic impression and heat generation/absorption. The unique boost in thermal efficiency and development of the rate of heat transport as valid to the dynamics of energy and coolant in automobiles is what has led to an increase in knowledge of hybrid nanofluid. For the study, two groups of ternary nanoparticles (*CNT*-*Gr*-Fe_3O_4 and MgO-Cu-Au) are combined with the base fluid kerosene oil. A nonlinear partial differential equation system is created while keeping in mind some reasonable presumptions. Using the similarities transformation, PDE's are changed into nonlinear ODE's. Also, it is then mathematically simplified with the bvp4c technique. The consequences of an exclusive group of unique impacts on motion characteristics, skin friction coefficient, thermal field impressions, heat transport rate, concentration distribution, and mass transfer rate are described clearly. The motion in the x and y directions decays with increasing the Casson fluid parameter $0.04 \leq \beta \leq 0.06$ and magnetic impact $(6 \leq M \leq 10)$ for ternary groups I and II. An energy upsurge profile appears for radiation impression $(1 \leq \mathrm{Nr} \leq 20)$ and heat source/sink $(0.1 \leq Q \leq 1.5)$. When compared to rising Dufour number $(0.1 \leq Du \leq 0.9)$ and heat source/sink values $(0.1 \leq Q \leq 1.5)$, the Nusselt number decreases. The volume fraction $(0.1 \leq \phi \leq 0.3)$ of ternary nanoparticles rises the velocity (in both directions) and thermal distributions. Also, the Nusselt number enhances for both ternary groups when increasing thermal radiation $(1 \leq \mathrm{Nr} \leq 20)$.

1. Introduction

Nanoliquid is a colloidal combination of regular liquids with particles by a diameter of nanometers. These particles are used to improve the thermal characteristics of common liquids with poor thermal conductivities. The most recent generations have employed numerous cutting-edge approaches to increase heat transfer rates to reach various rates of thermal capabilities. To accomplish this, improving heat conductivity is essential. In the end, various attempts to improve thermal conductivity were made by spreading larger thermally conductive solid components throughout the fluids. Various studies on nanofluids have been conducted to meet the demands of commercial applications. Nanofluids may quench the demand of energy utilization experts and scientists, but a better sort of fluid is still under investigation. To address them, better nanofluid forms with a higher thermal conductivity than nanofluid, such as "hybrid nanofluid" have arisen. These types of nanoparticles have high thermal properties. When we mix these types of nanoparticles, we get better thermal conductivity. Because of this, the current work's main objective is to increase heat rate transmission using a ternary hybrid nanofluid.

Nanofluid is utilized in a variety of industrial and nanotechnological techniques, including heat transfer systems, electronic device cooling, nuclear reactors, vehicle cooling, and vehicle thermal management, among others, to solve real-world challenges. Magnetic nanofluids are also useful for a wide range of other uses, including the treatment of wounds, the opening of blocked arteries, therapy for cancer, and magnetic resonance imaging. Ahmad et al. [1] explored the augmentation of Go/kerosene oil and Gr-silver/kerosene oil hybrid nanoliquids in the existence of an applied magnetic field if the liquids stream across a porous medium through a stretched surface. Kerosene oil- (Ko-) based hybrid nanofluid, a particular diathermal oil, was the subject of an examined by Anwar et al. [2]. The needed hybrid nanoliquid is created by the hybridization of MgO and silica nanoparticles. By creating a new combination of nanoparticles known as triple particles, Bilal et al. [3] explained the hydrothermal properties of water in this article. Two distinct kinds of groups are taken into account for this purpose: one with lower densities (CNT, Gr, and aluminum oxide) and the other with a greater density (CuO, Cu, and Ag). Elnaqeeb et al. [4] looked into the process of transport of water carrying lesser densities of tiny particles (such as CNT, Gr, and Al_2O_3) and significant higher densities of tiny particles (such as CuO, Cu, and Ag) of different kinds with a rectangular closed field. Deionized water- (DIW-) based Al_2O_3 and MWCNT mix nanoliquids were studied by Giwa et al. [5] to determine how temperatures and mass ratios of particles affected the fluids' viscosity and electrical conductivity. Huminic and Huminic [6] investigated the heat transmission capabilities and level of thermodynamic irreversibility of the two kinds of hybrid nanofluids, specifically MWCNT-Fe_3O_4/water and ND-Fe_3O_4/water, utilized in a flattened tube. A pair of emphasize based on water nanofluids, a mix nanoliquid, and thermal radiation in a triple mixed nanofluid was studied by Jakeer et al. [7] to determine how nonlinear Darcy–Forchheimer affected the electromagneto hydrodynamic flow of these fluids on a sheet that was stretched. One of the non-Newtonian fluid classes that established the properties of yield stress was the Casson liquid model. In real life, Casson fluid is frequently utilized in things like jelly, honey, sauce, concentrated fruit juices, and soup. Additionally, it has a wide range of applications in the domains of industries that advance daily. The non-Newtonian fluid presents a significantly more difficult study due to its dynamics, complexity, and interactions. Krishna [8] established with using into consideration account the impacts of heat generation and viscous dissipation, the impact of Newtonian heat on unstable an infinitely oscillating vertically plate attached to a porous medium is used to accomplish MHD free convective flow of a radiate and chemically reacting Casson mixed nanoliquid.

Majeed et al. [9] investigated the non-Newtonian (Casson) tiny liquids models: two-dimensional bioconvection MHD stream and warm transmission. To simulate the MHD Casson in two dimensions stream across a linearly extending/contracting sheet given the convective boundary conditions and suction, and radiation impacts, Mousavi et al. [10] investigated the thermal efficiency of a mix of water/MgO-Ag nanoliquid. Mahanta and Shaw [11] explored a porous, linear extended sheet is passed by a 3D Casson fluid in this issue using magneto hydrodynamics (MHD). Electromagnetic waves transmit energy or heat through a process called thermal radiation. When there is a significant variation in temperature between the boundary surfaces and the surrounding fluid, radiation parameter is crucial. Radiative influences are important in physics and engineering. When completing tasks involving high temperatures and space technology, consideration of radiation heat transfer's impacts on diverse flows is crucial. In addition, the impacts of radiation are crucial for observing heat transfer in the polymer sectors, where heat regulating components have a minimal impact on the final product's quality. The implications of radiation on airplanes, gas turbines, spacecraft, liquid metal fluids, and solar radiation are also pertinent. Mandal and Pal [12] studied the steady two-dimensional magneto hydrodynamic nature of stream and heat exchange of the Darcy–Forchheimer non-Newtonian (cross) mix nanoliquid made of Go/kerosene oil and Go-Ag/kerosene oil passing by the permeable medium through a stretch sheet. Nayak et al. [13] examined a three-dimensional GO-MoS_2/Casson combined nanofluid stream over two parallel plates is studied to determine how the magnetic field, nonlinear radiation impact, heat absorption, and viscous dissipation affect it. Nasir et al. [14] examined how radiation impression affected the flow of water-based nano, mix, and triple mix nanofluids under a couple stress on a sheet that was stretched. SiO_2, TiO_2, and Al_2O_3 nanoparticles are combined with the base fluid H_2O to form the triple hybrid nanofluid ($SiO_2 + TiO_2 + Al_2O_3/H_2O$).

The thermodiffusion and diffusion thermo impacts on Casson nanoliquid moving in a perpendicular system under the influence of radiation impact were studied by Patil et al. [15]. Titania-ethylene glycol nanofluid (TiO_2/EG NF) flow through a wedge with nanoparticle aggregation effect was investigated by Kumar Rawat et al. [16]. This flow occurred in the presence of suction/injection effects, mixed convection, thermal radiation, porous media, and nonuniform heat source/sink. The exchange of mass and energy processes of a 3D triple hybrid nanoliquid stream through a porous medium in the direction of an expanding surface were investigated by Ramzan et al. [17]. The impacts of thermos diffusion and diffusion thermo factors on the characteristics of a hybrid nanoliquid stream between the electric conductivity of two plates in parallel with depending on temperature were looked at by Revathi et al. [18]. Reddy et al. [19] quantitatively evaluated the impact of updated the energy flux of Fourier on the energy transmission characteristics of a mix nanoliquid made of MgO, magnetite (Fe_3O_4) as tiny particles, and ethylene glycol (Eg) as an ordinary liquid. The effects of the Cattaneo–Christov model (CC model) and quadratic thermal radiation with convective boundary conditions on ternary hybrid nanofluid (TiO_2-SiO_2-MoS_2/kerosene oil) flow across a spinning disc were investigated by Singh et al. [20]. Shaheen et al. [21] investigated the impact of varied parameters on the flow of a hazy Casson nanofluid in three dimensions (3D) across a deformable surface with two directions combined the energy of Arrhenius activation and chemical reaction. Sayed and Hosham [22] researched the moveable reactions of streamline sequences with their splitting in a peristaltic stream channel to transmit heat. This kind showed a porous filled tapering asymmetric microchannel carrying a Casson incompressible mix nanoliquid Au-Cu/blood. Sarada et al. [23] explored the movement of a curved stretched sheet with activation energy across a tripartite cross nanofluid graphene-CNT-silver with water original fluid. The experiment by Sandeep et al. [24] was carried out to consider the novel relevance of the nonlinear thermal radiation influence on the magneto hydrodynamic movement of the Casson mix nanoliquid induced through a curved, extending surface. Using the legendre wavelet collocation technique (LWCT), Gupta et al. [25] investigated the computational solution of magnetised GP-MoS_2/$C_2H_6O_2$-H_2O unsteady flow across a stretching surface. Upreti et al. [26] examined the nature of heat and mass transfer on a Casson nanofluid flowing in three dimensions over a Riga plate with a changed magnetic field, thermophoresis, and Brownian motion. The Casson nanofluid contains gyrotactic microorganisms. Ullah et al. [27] studied the Casson hybrid nanofluid (HN) (ZnO-Ag/Casson fluid), which is electrically conductive and flows stably along a two-directional stretchy sheet when a changing magnetic flux is applied. On a Riga plate with suction and injection implications, Zari et al. [28] explored the Casson nanofluid formulation due to Marangoni convection. Graphene oxide (GO) is the hard nanoparticles, and water and kerosene oil are used as the regular base fluids for nanoparticles. The effect of cross diffusion features in combined convection radiation Casson liquid stream on an exponential heated sheet was investigated by Zaigham Zia et al. [29].

Ahmed et al. [30] studied the heat transfer development in a square heat exchanger under constant heat flux conditions with the turbulent flow of innovative metal oxide-based ternary composite nanofluids of $ZnO + Al_2O_3 + TiO_2$/DW at varied weight percent concentrations (0.025, 0.05, 0.075, and 0.1). Mousavi et al. [31] explained the effects of nanoparticle volume concentration and temperature on the thermophysical characteristics and the rheological behaviour of water-based CuO/MgO/TiO_2 ternary hybrid nanofluids. An inclined catheterized artery with several stenoses and wall slip was examined by Dolui et al. [32] using ternary hybrid nanoparticles (Cu-Ag-Au). Nasir et al. [33] compared the effects of MHD, viscous dissipation, nonlinear thermal convection and radiation, joule heating, and the presence of a heat source over stretching surface on SiO_2/H_2O nanofluid, $TiO_2 + Al_2O_3$/H_2O hybrid nanofluid, and $SiO_2 + TiO_2 + Al_2O_3$/H_2O ternary hybrid nanofluid flow.

Inspired by the literature listed above, this work's primary objective is to fill this gap. The authors examined 3D non-Newtonian steady radiative MHD Casson ternary hybrid nanofluids flow across a dually stretch sheet with heat generation/absorption and viscous dissipation. For this aim, two ternary nanoparticles, namely, (CNT, graphene, and Fe_3O_4) and (MgO, Cu, and Au) are mixed with the base fluid kerosene oil. The results are generated using the bvp4c application. However, research into this flow over a dually stretching sheet has not yet started. We can be confident that the results of our computational work are applied to any real-time issues in a variety of thermal engineering fields, including energy production, heating and cooling systems, and the design of new thermal systems and medical science such as cancer therapy and industries.

2. Mathematical Formulation

We have supposed three-dimensional, time-independent, viscous, incompressible boundary layer MHD non-Newtonian Casson ternary hybrid nanofluids flow over a bidirectional stretching sheet. The fluid layer's stretching velocities along the x and y axes adjacent to the horizontal surfaces are $u_w(x) = ax$ and $v_w(x)$ = by, correspondingly. The wall temperature and concentration are T_w and C_w, consequently (see Figure 1). Additionally, the following flow presumptions are noted for the present analysis:

(i) Two ternary nanoparticles: one kind is CNT, graphene, and Fe_3O_4, and the other is MgO, Cu, and Au
(ii) Base fluid-kerosene oil
(iii) Radiation impact, magnetic parameter, viscous dissipation, and heat source/sink

Non-Newtonian Casson fluid's constitutional relationships are used [8, 12, 13]

$$\tau_{mn} = \begin{cases} 2\left(\mu_B + \dfrac{\tau_y}{\sqrt{2\pi}}\right)e_{mn}, & \pi > \pi_c, \\ \\ 2\left(\mu_B + \dfrac{\tau_y}{\sqrt{2\pi}}\right)e_{mn}, & \pi < \pi_c, \end{cases} \tag{1}$$

where $\pi = e_{mn}e_{mn}$ and e_{mn} is the $(m, n)^{Th}$ portion relating to rate of deformation, π is the multiple of the sections of defacement amount, π_c is essential value of the multiply founded by fluid with non-Newtonian behaviour, μ_B is the non-Newtonian fluid's plastic moveable viscosity, and τ_y is yield stress for the fluid.

The continuity, motion, temperature, and concentration hybrid nanofluids controlling boundary layer equations are expressed as follows [3]:

Equation of continuity is stated as follows:

$$\frac{\partial u}{\partial x} + \frac{\partial v}{\partial y} + \frac{\partial w}{\partial z} = 0. \tag{2}$$

Equation of motion is stated as follows:

$$\begin{aligned} u\frac{\partial u}{\partial x} + v\frac{\partial u}{\partial y} + w\frac{\partial u}{\partial z} &= \frac{\mu_{\mathrm{hbnf}}}{\rho_{\mathrm{hbnf}}}\left(1 + \frac{1}{\beta}\right)\frac{\partial^2 u}{\partial z^2} - \frac{\sigma_{\mathrm{hbnf}}}{\rho_{\mathrm{hbnf}}}B_0^2 u, \\ u\frac{\partial v}{\partial x} + v\frac{\partial v}{\partial y} + w\frac{\partial v}{\partial z} &= \frac{\mu_{\mathrm{hbnf}}}{\rho_{\mathrm{hbnf}}}\left(1 + \frac{1}{\beta}\right)\frac{\partial^2 v}{\partial z^2} - \frac{\sigma_{\mathrm{hbnf}}}{\rho_{\mathrm{hbnf}}}B_0^2 v. \end{aligned} \tag{3}$$

Equation of temperature is stated as follows:

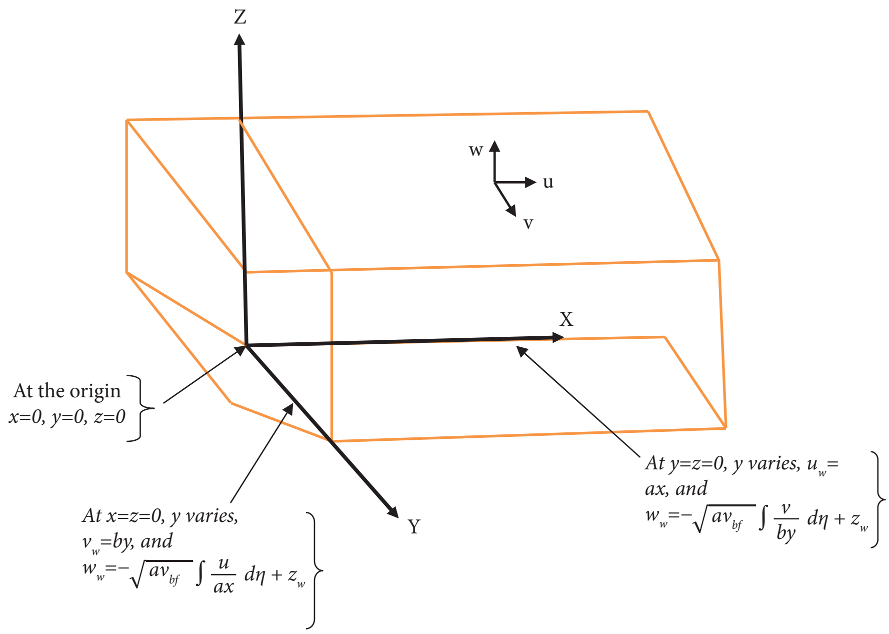

Figure 1: Physical configuration of the flow problem.

$$u\frac{\partial T}{\partial x}+v\frac{\partial T}{\partial y}+w\frac{\partial T}{\partial z}=\frac{k_{\mathrm{hbnf}}}{\left(\rho C_p\right)_{\mathrm{hbnf}}}\frac{\partial^2 T}{\partial z^2}+\frac{\mu_{\mathrm{hbnf}}}{\left(\rho C_p\right)_{\mathrm{hbnf}}}\left(1+\frac{1}{\beta}\right)\left(\frac{\partial u}{\partial z}\right)^2-\frac{1}{\left(\rho C_p\right)_{\mathrm{hbnf}}}\frac{\partial q_r}{\partial z}+\frac{D_m K_T}{C_s C_p}\frac{\partial^2 C}{\partial z^2}+\frac{Q_0}{\left(\rho C_p\right)_{\mathrm{hbnf}}}\left(T-T_\infty\right). \tag{4}$$

Equation of concentration is stated as follows:

$$u\frac{\partial C}{\partial x}+v\frac{\partial C}{\partial y}+w\frac{\partial C}{\partial z}=D_m\frac{\partial^2 C}{\partial z^2}-\mathrm{k}_1\left(\mathrm{C}-\mathrm{C}_\infty\right)+\frac{\mathrm{D_m K_T}}{\mathrm{T_m}}\frac{\partial^2 \mathrm{T}}{\partial \mathrm{z}^2}. \tag{5}$$

The associate borderline circumstances are composed by the following equation [3, 4]:

$$\begin{aligned}
&u=u_w(x)=ax, w=w_w=\left(-\sqrt{av_{bf}}\int\frac{v}{ay}d\eta+z_w\right)\text{at } z=0, \text{and } y=0,\\
&v=v_w(x)=by, w=w_w=\left(-\sqrt{av_{bf}}\int\frac{u}{ax}d\eta+z_w\right)\text{at } z=0 \text{ and } x=0,\\
&T=T_w, C=C_w, \text{at } z=0,\\
&\qquad u\longrightarrow 0, \text{at } z\longrightarrow\infty \text{ and } y=0, v\longrightarrow 0, \text{at } z\longrightarrow\infty \text{ and } x=0,\\
&\qquad T\longrightarrow T_\infty, C\longrightarrow C_\infty, \text{at } z\longrightarrow\infty.
\end{aligned} \tag{6}$$

The motion coefficient in x and y consistent coordinates, indicated by u and v, serially, where the fluid temperature is T (Kelvin – K) and β is several the shear thinning Casson fluid. Furthermore, *hbnf* denotes hybrid nanofluid, bf indicates base fluid, $(\rho C_p)_{\mathrm{hbnf}}$ stands for the hybrid nanofluid's capability for heat, B_0 (Tesla-T) denotes the power of the magnetic impact, σ_{hbnf} depicts the electrical conductivity of the hybrid nanoliquid, k_{hbnf} stands for the hybrid nanoliquid thermal conductivity, ρ_{hbnf} depicts the density of the mixed nanofluid, μ_{hbnf} denotes the dynamic viscosity of mix nanoliquid, z_w is suction rate, Q_0 stands inside heat source (>0)/sink (<0) amount, D_m denotes diffusivity, the chemical reactive parameter define as k_1, C is the concentration, $C_p$is the heat capacity at stable pressure, and C_s represents for the concentration susceptibility.

Here, ϕ_1 represents the concentration of first nanoparticles, ϕ_2 is the volume fraction of second nanoparticles, ϕ_3 denotes the volume fraction of third nanoparticles, and nf denotes the nanoparticles. Electrical conductivity, dynamic viscosity, density, and thermal conductivity of the original fluid denotes $k_{\text{bf}}, \mu_{\text{bf}}, \rho_{\text{bf}}$, and σ_{bf} serially. In light of this, Table 1 provides details on the operating pure fluid and ternary nanostructures (see Table 2).

In energy equation (4), the Rosseland term, where q_r denotes the flux of radiant heat and is determined using the Rosseland estimation, corresponds to thermal radiation [9, 11, 14, 15, 24].

$$q_r = \frac{-4\sigma}{3k^*}\frac{\partial T^4}{\partial z}, \tag{7}$$

where k^* stands for the coefficient of mean absorption and σ is the Stefan–Boltzmann constant. Currently, utilizing the Taylor series T^4 as the reference at a position T_∞ and neglecting the approximate greater-order expressions and we can get the final form listed below:

Inscribe the T^4 as a liner relation of temperature with Taylor series extension about T_∞ and disregarding superior expressions, we obtain the following equation:

$$T^4 \approx 4T_\infty^3 T - 3T_\infty^4. \tag{8}$$

In the recent situation, by using the following transformations listed as follows [3], equations that are dimensional are transformed into nondimensional equations.

$$\eta = z\sqrt{\frac{a}{\nu_{\text{bf}}}}, u = \text{ax}f'(\eta), v = \text{by}, g'(\eta), w = -\sqrt{a\nu_{\text{bf}}}\,[f(\eta) + cg(\eta)], \theta(\eta) = \frac{T - T_\infty}{T_w - T_\infty}, \phi(\eta) = \frac{C - C_\infty}{C_w - C_\infty}, \tag{9}$$

where the primes represent differentiation of the pseudo-similarity variables.

The nondimensional form of equations is obtained by applying transformations, and it is as follows:

$$\frac{\mu_{\text{hbnf}}/\mu_{\text{bf}}}{\rho_{\text{hbnf}}/\rho_{\text{bf}}}\left(1 + \frac{1}{\beta}\right)f''' + (f + \text{cg})f'' - f'^2 - \frac{\sigma_{\text{hbnf}}/\sigma_{\text{bf}}}{\rho_{\text{hbnf}}/\rho_{\text{bf}}}Mf' = 0, \tag{10}$$

$$\frac{\mu_{\text{hbnf}}/\mu_{\text{bf}}}{\rho_{\text{hbnf}}/\rho_{\text{bf}}}\left(1 + \frac{1}{\beta}\right)g''' + (f + \text{cg})g'' - cg'^2 - \frac{\sigma_{\text{hbnf}}/\sigma_{\text{bf}}}{\rho_{\text{hbnf}}/\rho_{\text{bf}}}Mg' = 0, \tag{11}$$

$$\frac{((k_{\text{hbnf}}/k_{\text{bf}})+\text{Nr})}{(\rho C_p)_{\text{hbnf}}/(\rho C_p)_{\text{bf}}}\theta'' + \Pr(f + \text{cg})\theta' + \frac{1}{(\rho C_p)_{\text{hbnf}}/(\rho C_p)_{\text{bf}}}\text{PrQ}\theta + \frac{\mu_{\text{hbnf}}/\mu_{\text{bf}}}{(\rho C_p)_{\text{hbnf}}/(\rho C_p)_{\text{bf}}}\left(1 + \frac{1}{\beta}\right)\text{Ec}f''^2 + \text{DuPr}\phi'' = 0, \tag{12}$$

$$\phi'' - \text{KrSc}\phi + \text{Sc}(f + \text{cg})\phi' + \text{ScSr}\theta'' = 0. \tag{13}$$

With suitable boundary circumstances,

$$\begin{aligned} &f(0) = f_w, f'(0) = 1, g(0) = \frac{f_w}{c}, g'(0) = 1, \theta(0) = 1, \phi(0) = 1 \text{ at } \eta = 0,\\ &f'(\infty) \longrightarrow 0, g'(\infty) \longrightarrow 1, \theta(\infty) \longrightarrow 0, \phi(\infty) \longrightarrow 0 \text{ at } \eta \longrightarrow \infty. \end{aligned} \tag{14}$$

The expressions used to indicate the presence of dimensionless limitations in equations (10)–(14) are the non – Newtonian Casson parameter (β), magnetic parameter or Hartmann parameter (M), chemical reaction (Kr), Eckert number (Ec), Soret impact (Sr), Schmidt number (Sc), Prandtl parameter (Pr), radiation parameter (Nr), Dufour impact (Du), nondimensional suction parameter (f_w), ratio of stretching speed (c), and heat generation/absorption (Q). These factors are listed numerically as follows:

Table 1: The thermophysical properties of the hybrid nanofluid [3, 4, 7].

Thermal properties	Hybrid nanofluid
Thermal diffusivity	$\alpha_{\text{hbnf}} = k_{\text{hbnf}}/(\rho C_p)_{\text{hbnf}}$
Viscosity	$\mu_{\text{hbnf}} = \mu_{nf1}\phi_1 + \mu_{nf2}\phi_2 + \mu_{nf3}\phi_3/(1-\phi_1-\phi_2-\phi_3)^{2.5}$ $\mu_{\text{hbnf}}/\mu_{\text{bf}} = 1/(1-\phi_1-\phi_2-\phi_3)^{2.5}$
Heat capacity	$(\rho C_p)_{\text{hbnf}} = (1-\phi_1-\phi_2-\phi_3)(\rho C_p)_{\text{bf}} + (\rho C_p)_{\text{nf1}}\phi_1 + (\rho C_p)_{\text{nf2}}\phi_2 + (\rho C_p)_{\text{nf3}}\phi_3$ $(\rho C_p)_{\text{hbnf}}/(\rho C_p)_{\text{bf}} = \phi_1(\rho C_p)_{\text{nf1}}/(\rho C_p)_{\text{bf}} + \phi_2(\rho C_p)_{\text{nf2}}/(\rho C_p)_{\text{bf}} +$ $\phi_3(\rho C_p)_{\text{nf3}}/(\rho C_p)_{\text{bf}} + (1-\phi_1-\phi_2-\phi_3)$
Density	$\rho_{\text{hbnf}} = (1-\phi_1-\phi_2-\phi_3)\rho_{\text{bf}} + \rho_{\text{nf1}}\phi_1 + \rho_{\text{nf2}}\phi_2 + \rho_{\text{nf3}}\phi_3$ $\rho_{\text{hbnf}}/\rho_{\text{bf}} = \phi_1\rho_{\text{nf1}}/\rho_{\text{bf}} + \phi_2\rho_{\text{nf2}}/\rho_{\text{bf}} + \phi_3\rho_{\text{nf3}}/\rho_{\text{bf}} + (1-\phi_1-\phi_2-\phi_3)$
Thermal conductivity	$k_{\text{hbnf}}/k_{\text{bf}} = (\phi_1 k_{nf1} + \phi_2 k_{nf2} + \phi_3 k_{nf3}/\phi_{\text{hbnf}} + 2k_{\text{bf}} + 2(\phi_1 k_{\text{nf1}} + \phi_2 k_{\text{nf2}} + \phi_3 k_{\text{nf3}}) -$ $2\phi_{\text{hbnf}}k_{\text{bf}}/\phi_1 k_{\text{nf1}} + \phi_2 k_{\text{nf2}} + \phi_3 k_{\text{nf3}}/\phi_{\text{hbnf}} + 2k_{\text{bf}} - (\phi_1 k_{\text{nf1}} + \phi_2 k_{\text{nf2}} + \phi_3 k_{\text{nf3}}) +$ $\phi_{\text{hbnf}}k_{\text{bf}})$
Electrical conductivity	$\sigma_{\text{hbnf}}/\sigma_{\text{bf}} = (\phi_1\sigma_{\text{nf1}} + \phi_2\sigma_{\text{nf2}} + \phi_3\sigma_{\text{nf3}}/\phi_{\text{hbnf}} + 2\sigma_{\text{bf}} + 2(\phi_1\sigma_{\text{nf1}} + \phi_2\sigma_{\text{nf2}} + \phi_3\sigma_{\text{nf3}}) -$ $2\phi_{\text{hbnf}}\sigma_{\text{bf}}/\phi_1\sigma_{\text{nf1}} + \phi_2\sigma_{\text{nf2}} + \phi_3\sigma_{\text{nf3}}/\phi_{\text{hbnf}} + 2\sigma_{\text{bf}} - (\phi_1\sigma_{\text{nf1}} + \phi_2\sigma_{\text{nf2}} + \phi_3\sigma_{\text{nf3}}) + \phi_{\text{hbnf}})$

Table 2: Physical characteristics of two ternary nanoparticles/kerosene oil hybrid nanoparticles [2–4, 19, 22].

Hybrid nanofluids	ρ (kg·m^{-3})	C_p (JK^{-1}·kg^{-1})	K (w·m^{-1}·K^{-1})	σ (Ω^{-1}m^{-1})	Pr
Kerosene oil	783	2090	0.145	21×10^{-6}	21
CNT (carbon nanotube)	2100	410	3007.4	1569.5×10^{7}	—
Graphene	2200	790	5000	1×10^{7}	—
Fe_3O_4	3970	765	40	25×10^{3}	—
MgO (magnesium oxide)	3.57	0.852	5.112	1.42×10^{-3}	—
Cu (copper)	8933	385	400	59.6×10^{6}	—
Au (gold)	19300	129	318	4.1×10^{6}	—

$$\beta = \mu_B\frac{\sqrt{2\pi_C}}{\tau_y}, M = \frac{\sigma_{\text{bf}}B_0{}^2}{\rho_{\text{bf}}a}, c = \frac{b}{a}, \text{Pr} = \frac{(\mu c_p)_{\text{bf}}}{k_{\text{bf}}}, \text{Ec} = \frac{a^2x^2}{(C_p)_{\text{bf}}(T_w - T_\infty)}, \text{Nr} = \frac{16\sigma T_\infty^3}{3k_{\text{bf}}k^*},$$
$$Q = \frac{Q_0}{a(\rho C_p)_{\text{bf}}}, \text{Du} = \frac{D_m K_T(C_w - C_\infty)}{\nu_{\text{bf}}C_s C_p(T_w - T_\infty)}, \text{Kr} = \frac{k_1}{a}, \text{Sr} = \frac{D_m K_T(T_w - T_\infty)}{T_m\nu_{\text{bf}}(C_w - C_\infty)}, \text{Sc} = \frac{\nu_{\text{bf}}}{D_m}, f_w = -\frac{z_w}{\sqrt{a\nu_{\text{bf}}}}. \tag{15}$$

2.1. Physical Quantities

2.1.1. Skin Friction Number. The precise definition of the physical quantity of skin friction (C_f) that arises as a result of the viscous stretch around the plate is $C_f = \tau_w/\rho_{\text{bf}}u_w^2$, where surface shear stress is τ_w, which is implied by $\tau_w = \mu_{\text{hbnf}}(1 + 1/\beta)(\partial u/\partial z)_{z=0}$

The dimensional form of the skin friction factors along the x and y directions are shown as follows:

$$C_{\text{fx}} = \frac{\mu_{\text{hbnf}}}{\rho_{\text{bf}}a^2x^2}\left(1 + \frac{1}{\beta}\right)\left(\frac{\partial u}{\partial z}\right)_{z=0},$$
$$C_{\text{fy}} = \frac{\mu_{\text{hbnf}}}{\rho_{\text{bf}}b^2y^2}\left(1 + \frac{1}{\beta}\right)\left(\frac{\partial v}{\partial z}\right)_{z=0}. \tag{16}$$

2.1.2. Heat Transfer Rate. The Nusselt number along the x and y directions are cleared like $\text{Nu}_x = xq_w/k_{\text{bf}}(T_w - T_\infty)$, $\text{Nu}_y = yq_w/k_{\text{bf}}(T_w - T_\infty)$, where $q_w$is signifies heat flux, which is described asfollows:

$$q_w = -k_{\text{hbnf}}\left(\frac{\partial T}{\partial z}\right)_{z=0} + (q_r)_{z=0}. \tag{17}$$

2.1.3. Mass Transfer rate. A Sherwood parameter (Sh) that is assumed yields the quantity of mass movement. This is defined as $Sh_x = xq_m/D_m(C_w - C_\infty)$, the mass transfer amount at the wall is q_m, which is described as follows:

$$q_m = -D_m\left(\frac{\partial C}{\partial z}\right)_{z=0}. \tag{18}$$

Therefore, in terms of equations (16)–(18), the following nondimensional quantities are obtained:

$$C_{\text{fx}}\text{Re}_x^{1/2} = \left(\frac{\mu_{\text{hbnf}}}{\mu_{\text{bf}}}\right)\left(1 + \frac{1}{\beta}\right)f''(0),$$
$$C_{\text{fy}}Re_y^{1/2} = \left(\frac{\mu_{\text{hbnf}}}{\mu_{\text{bf}}}\right)\left(1 + \frac{1}{\beta}\right)g''(0), \tag{19}$$
$$\text{Nu}_x\text{Re}_x^{-1/2} = \text{Nu}_y\text{Re}_y^{-1/2} = \left[\left(\frac{-k_{\text{hbnf}}}{k_{\text{bf}}}\right) + \text{Nr}\theta'\right](0),$$

$Sh_x\text{Re}_x{}^{-1/2} = Sh_y\text{Re}_y{}^{-1/2} = -\phi'(0)$, where $\text{Re}_x = ax^2/\nu_{\text{bf}}$ and $\text{Re}_y = b^2y^2/a\nu_{\text{bf}}$ are the Reynolds numbers in the x and y directions, respectively.

2.2. Numerical Scheme. Using the bvp4c method, equations are made simpler. All numerical data and graph are drawn using MATLAB software, which is explained in tables and graphs. The flowchart of the bvp4c method is presented in Figure 2.

$$f = y(1), f' = y(2), f'' = y(3), g = y(4), g' = y(5), g'' = y(6),$$
$$\theta = y(7), \theta' = y(8), \phi = y(9), \phi' = y(10). \tag{20}$$

The issues (10) through (14) transform into the following new form:

$$\begin{aligned}
&\frac{\mu_{\mathrm{hbnf}}/\mu_{\mathrm{bf}}}{\rho_{\mathrm{hbnf}}/\rho_{\mathrm{bf}}}\left(1+\frac{1}{\beta}\right)f''' + (y(1)+cy(4))y(3) - \frac{\sigma_{\mathrm{hbnf}}/\sigma_{\mathrm{bf}}}{\rho_{\mathrm{hbnf}}/\rho_{\mathrm{bf}}}My(2) - (y(2))^2 = 0,\\
&\cdot\frac{\mu_{\mathrm{hbnf}}/\mu_{\mathrm{bf}}}{\rho_{\mathrm{hbnf}}/\rho_{\mathrm{bf}}}\left(1+\frac{1}{\beta}\right)g''' + (y(1)+cy(4))y(6) - \frac{\sigma_{\mathrm{hbnf}}/\sigma_{\mathrm{bf}}}{\rho_{\mathrm{hbnf}}/\rho_{\mathrm{bf}}}My(5) - c(y(5))^2 = 0,\\
&\cdot\left(\frac{((k_{\mathrm{hbnf}}/k_{\mathrm{bf}})+\mathrm{Nr})}{(\rho C_p)_{\mathrm{hbnf}}/(\rho C_p)_{\mathrm{bf}}} - \mathrm{DuPrScsr}\right)\theta'' + \Pr(y(1)+\mathrm{c}y(4))y(8) + \mathrm{DuPrScKr}y(9) - \mathrm{DuPrSc}(y(1)\\
&+cy(4))y(10) + \frac{1}{(\rho C_p)_{\mathrm{hbnf}}/(\rho C_p)_{\mathrm{bf}}}\mathrm{PrQ}y(7) + \frac{\mu_{\mathrm{hbnf}}/\mu_{\mathrm{bf}}}{(\rho C_p)_{\mathrm{hbnf}}/(\rho C_p)_{\mathrm{bf}}}\left(1+\frac{1}{\beta}\right)\mathrm{Ec}(y(3))^2 = 0,\\
&\cdot\left(1 - \mathrm{DuPrScSr}\frac{(\rho C_p)_{\mathrm{hbnf}}/(\rho C_p)_{\mathrm{bf}}}{((k_{\mathrm{hbnf}}/k_{\mathrm{bf}})+\mathrm{Nr})}\right)\phi'' + \mathrm{Sc}(y(1)+\mathrm{c}y(4))y(10)\\
&- \mathrm{ScKr}y(9) - \mathrm{SrPrSc}y(8)(y(1)+\mathrm{c}y(4))\frac{(\rho C_p)_{\mathrm{hbnf}}/(\rho C_p)_{\mathrm{bf}}}{((k_{\mathrm{hbnf}}/k_{\mathrm{bf}})+\mathrm{Nr})}\\
&+\frac{1}{((k_{\mathrm{hbnf}}/k_{\mathrm{bf}})+\mathrm{Nr})}\mathrm{ScSrPrQ}y(7) + \frac{\mu_{\mathrm{hbnf}}/\mu_{\mathrm{bf}}}{(k_{\mathrm{hbnf}}/k_{\mathrm{bf}})+\mathrm{Nr}}\left(1+\frac{1}{\beta}\right)\mathrm{ScSrEc}(y(3))^2 = 0.
\end{aligned} \tag{21}$$

Along with the boundary conditions in problem,

$$y0(1) = f_w, y0(2) = 1, y0(4) = \frac{f_w}{c}, y0(5) = 1, y0(7) = 1, y0(9) = 1 \text{ at } \eta = 0,$$
$$y\infty(2) \longrightarrow 0, y\infty(5) \longrightarrow 0, y\infty(7) \longrightarrow 0, y\infty(9) \longrightarrow 0 \text{ at } \eta \longrightarrow \infty. \tag{22}$$

The option $\eta(\infty) = 10, 3$ or 2.5 demonstrates that every numerical output in this method approaches asymptotic assets optimally.

2.3. Flowchart. The flowchart of Bvp4c function is as follows.

2.4. Code Validation. The use of comparison to recent research is used to validate the current findings. Comparing the known study consistencies is presented in Table 3. For the present analysis, however, extremely precise results are obtained.

3. Result and Discussion

Inside this section, the bvp4c method is used to evaluate the properties of various kerosene oil-based nanofluids, particularly *CNT*-*Gr*-Fe_3O_4/kerosene oil and MgO-Cu-Au/kerosene oil. We discuss the effects of flow parameters on motion in x and y directions, temperature, concentration, skin friction coefficients ($C_{f_x}\mathrm{Re}_x^{1/2}$ and $C_{f_y}\mathrm{Re}_y^{1/2}$), Nusselt number, and mass transfer coefficients. According to our measurements, the physical features for Figures 1–20 are as follows: $\Pr = 21, \beta = 0.06, M = 6, f_w = 0.3$, Nr = 1, Ec = 0.5, Kr = 0.5, Sc = 0.7, $c = 4$, Du = 0.5, Sr = Q = 0.1 and $\phi_1 = \phi_2 = 0.15$, $\phi_3 = 0.01$.

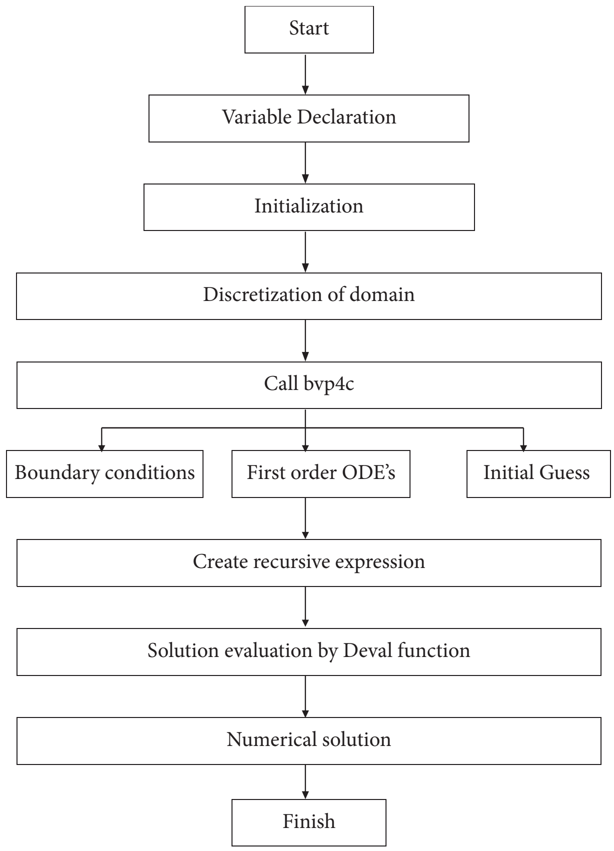

Figure 2: Flowchart of Bvp4c function.

Table 3: Assessment regarding the characteristics of $-\theta'(0)$ when $c = 0.3$, $f_w = 0.3$, $\phi\mu_{\mathrm{hbnf}}/\mu_{\mathrm{bf}}/\rho_{\mathrm{hbnf}}/\rho_{\mathrm{bf}} = \phi(k_{\mathrm{hbnf}}/k_{\mathrm{bf}})/(\rho C_p)_{\mathrm{hbnf}}/(\rho C_p)_{\mathrm{bf}} = 1$.

Pr	Bilal et al. [3]	Present work $(-\theta'(\mathbf{0}))$
0.2	0.1691	0.16915
0.7	0.4539	0.45381
2	0.9144	0.91428
7	1.8953	1.89537

Figures 3 and 4 show the velocity profiles in horizontal and vertical directions alongside the different value of Casson fluid parameter β for both ternary groups I and II. When we increase the value of the Casson fluid parameter, velocities significantly decrease for ternary group II in comparison to ternary group I due to a greater reduction in the thickness of the boundary layer for ternary group II. In Figures 5 and 6, the declines velocity $f'(\eta)$ and $g'(\eta)$ are displayed with rising magnetic parameter. The Lorentz force increases due to an increasing magnetic parameter, which increases the resistance in the fluid, so the velocity decreases more for ternary group II than for ternary group I. Since Lorenz force is inversely proportional to electrical conductivity, for ternary group II, the electrical conductivity is lower than for ternary group I.

Sketches of both Figures 7 and 8 are used to explain how suction velocity (f_w) affects the horizontal velocity (f') and vertical velocity (g'). It is observed that as the value of

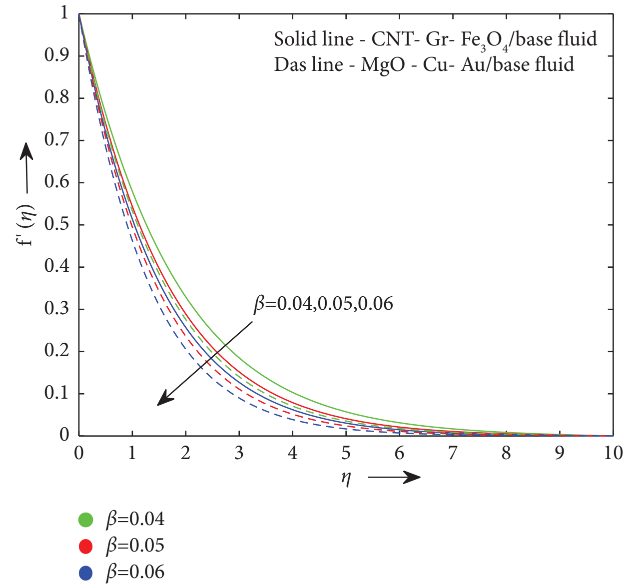

Figure 3: Velocity distribution $f'(\eta)$ for Casson fluid parameter β.

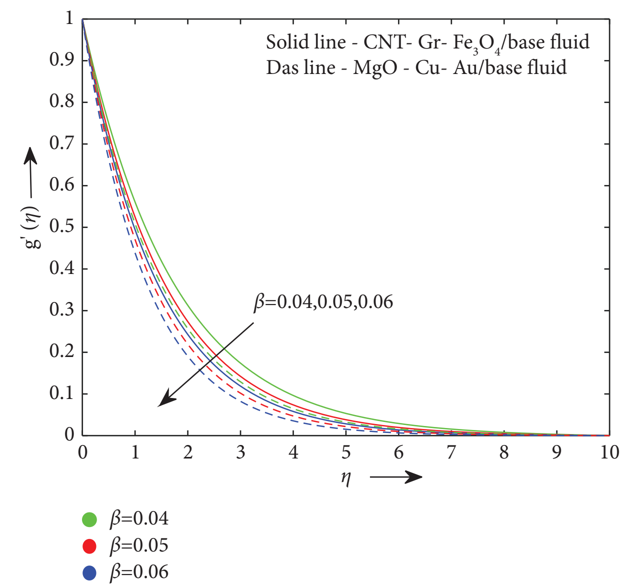

Figure 4: Velocity distribution $g'(\eta)$ for Casson fluid parameter β.

suction velocity rises, the motion distribution declines due to the given relation $f_w = -z_w/\sqrt{a\vartheta_{\mathrm{bf}}}$ for both ternary groups.

Furthermore, from Figures 9 and 10, it is concluded that a larger value of the stretching ratio parameter narrows the thermal and concentration distributions for both ternary groups I and II. For ternary groups I and II, Figure 11 depicts how the temperature grows as the amount of the radiation parameter Nr rises. The coefficient of heat absorption decreases as thermal radiation increases, raising the fluid temperature. As a result, because of the greater amount of heat transmitted there due to better radiation, the area's temperature increases. As can be illustrated from Figure 12, temperature distribution diminishes as the Prandtl number enhances for ternary groups I and II. We know that the

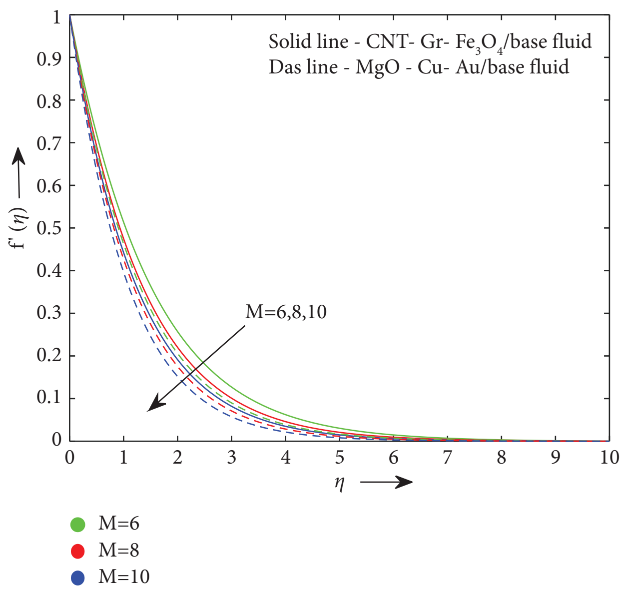

Figure 5: Velocity distribution in x direction for magnetic parameter M.

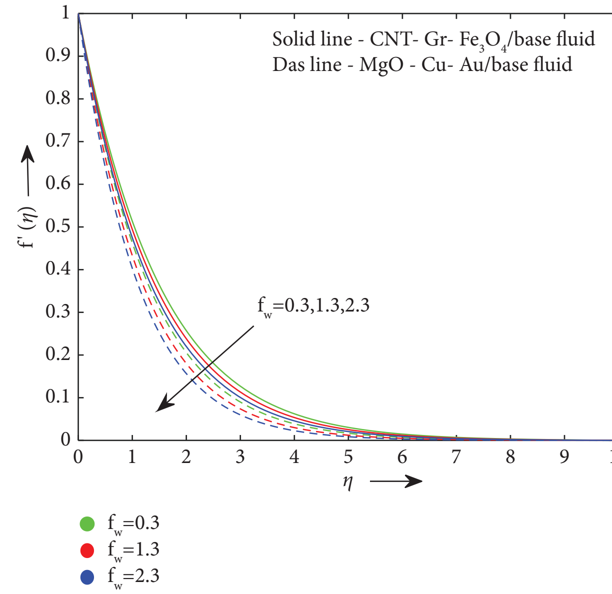

Figure 7: Velocity distribution $f'(\eta)$for suction velocity f_w.

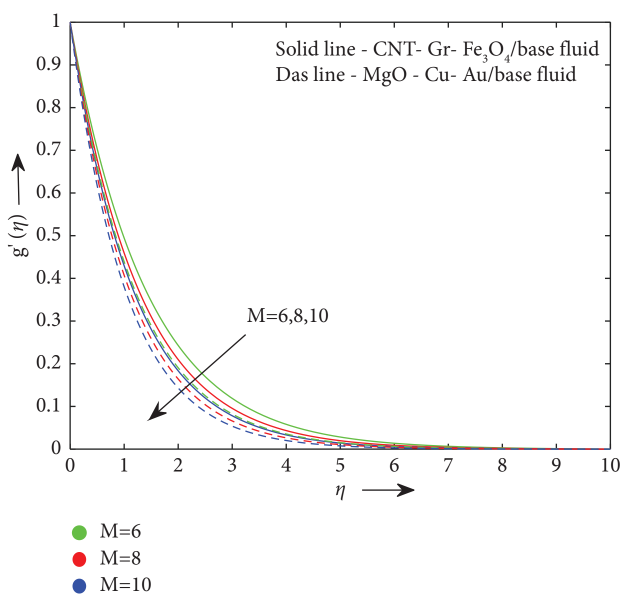

Figure 6: Velocity distribution in vertical direction for magnetic parameter M.

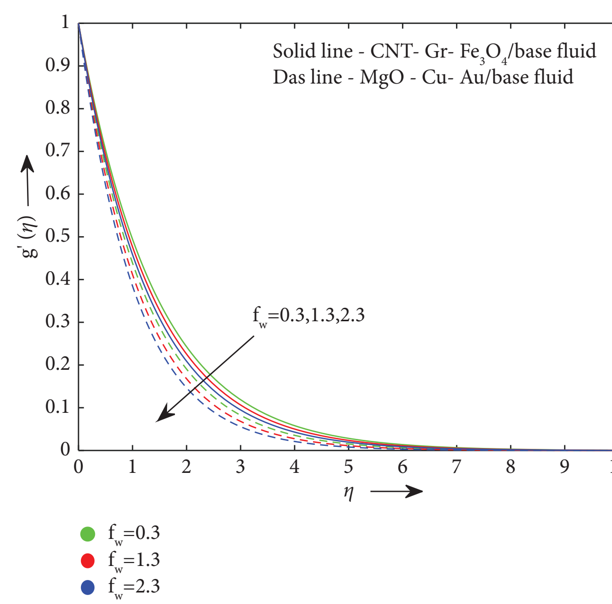

Figure 8: Velocity distribution $g'(\eta)$ for suction velocity f_w.

Prandtl parameter is the ratio of kinematic viscosity to temperature diffusivity. Since the mass and temperature diffusivities of nanoparticles decrease as Pr grows, the temperature of the fluid decreases.

The impact of the Eckert number Ec on $\theta(\eta)$ is apparent in Figure 13. Due to the enhancement in Eckert number, the process of converting mechanical energy into heat energy becomes quicker, due to which the temperature of the fluid rises. The Eckert number explains the connection between the flow of kinetic energy and the change in heat enthalpy. It indicates that as Eckert number grows, the hybrid nanofluids kinetic energy increases. Additionally, the average kinetic energy is a prevalent definition of temperature. Because of this, increasing the Eckert number enhances the temperature for ternary groups I and II. Figure 14 shows the drop in concentration with increasing values of the chemical reaction. Also, there are no significant differences in the levels of the concentration graphs for both the ternary groups. The diminishing effect of Sc on the concentration distribution is shown in

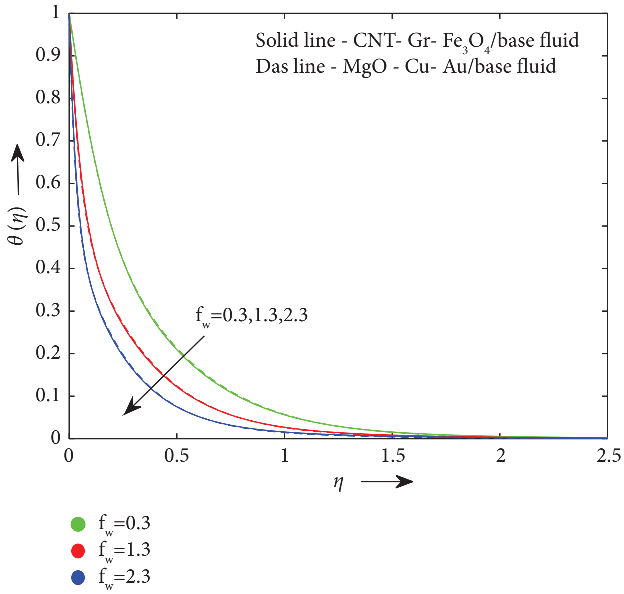

Figure 9: Temperature distribution for suction velocity f_w.

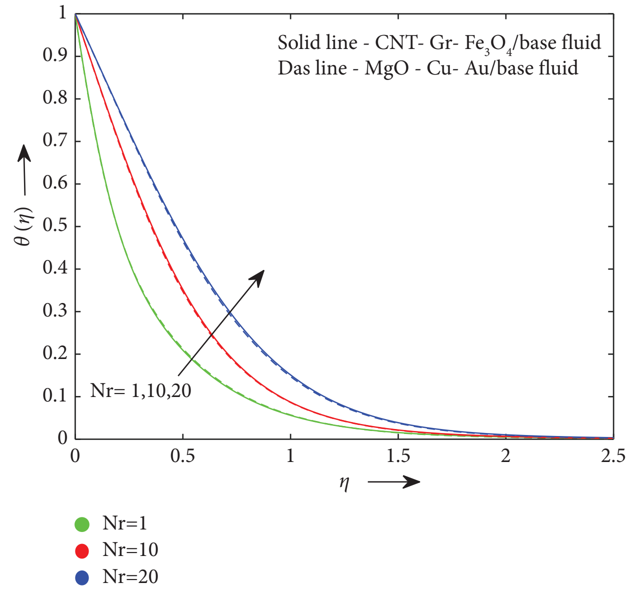

Figure 11: Temperature distribution for radiation parameter Nr.

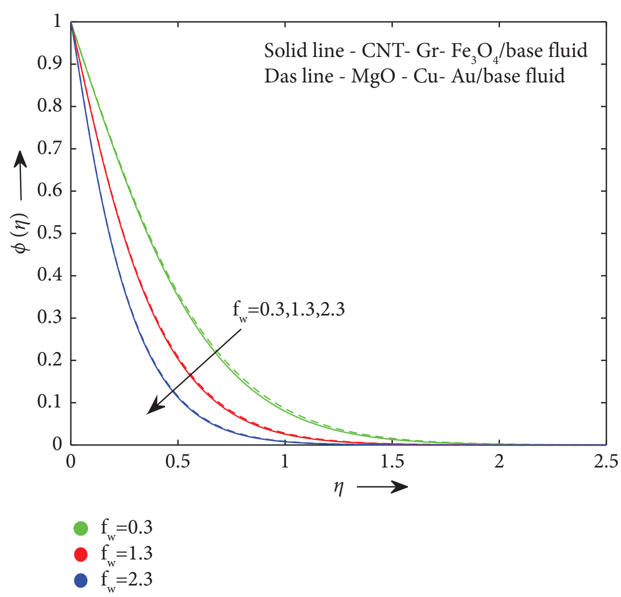

Figure 10: Concentration profile for suction velocity f_w.

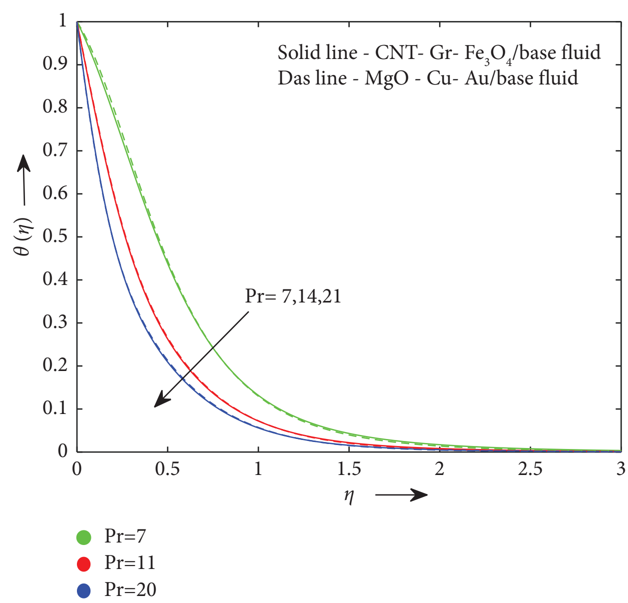

Figure 12: Temperature distribution for Prandtl number Pr.

Figure 15. This is because as the Schmidt number (Sc) increases, viscous diffusion increases, causing particles to travel wider and the convection potential to increase. Also, the concentration level decrease for both ternary groups. The influence of Du on the thermal field is exposed in Figure 16. The temperature field enlarges for greater values of Du for ternary groups I and II. This can be explained as an enlargement in the Dufour effect due to an enhancement in the concentration gradient and the rate of mass diffusion. As a result of which the heat transfer rate associated with the particles increases. Also, the thermal profile improves. Figure 17 displays how the concentration profile changes due to the Soret impact Sr. as the Soret number enlarges, the mass diffusion caused by temperature distribution also rises, which accelerates the rate of mass transport from the surface, so concentration increases for both ternary groups. Figure 18 illustrates how the thermal profile enlarges with the rising value of heat generation/

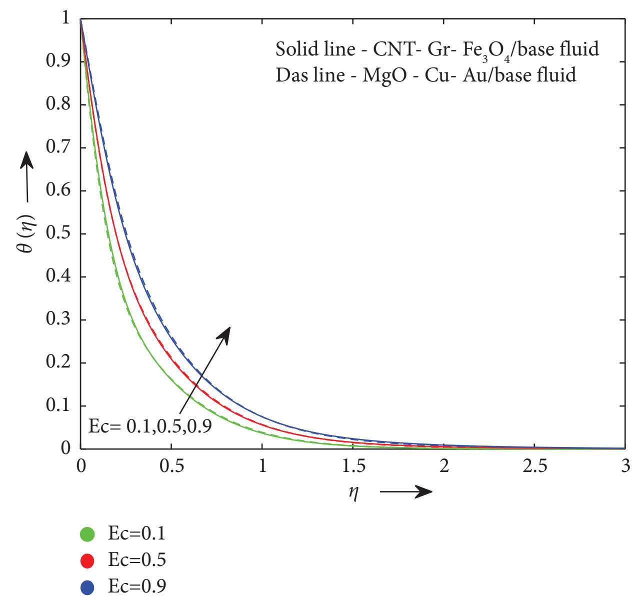

Figure 13: Temperature distribution for Eckert number Ec.

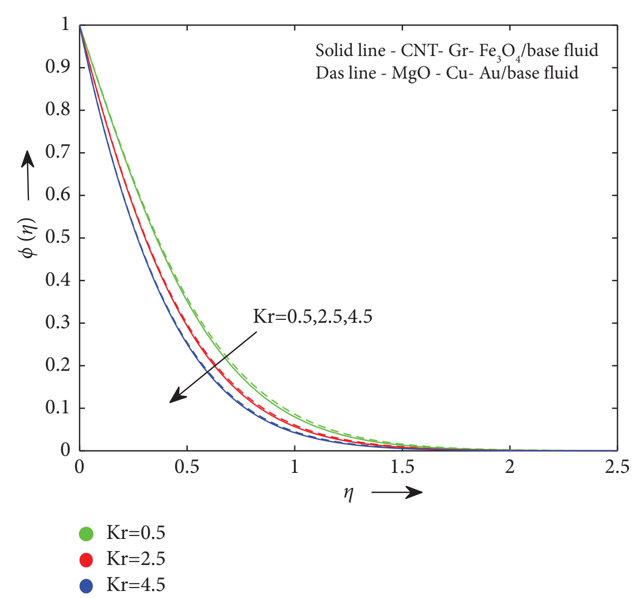

Figure 14: Concentration profile for chemical reaction Kr.

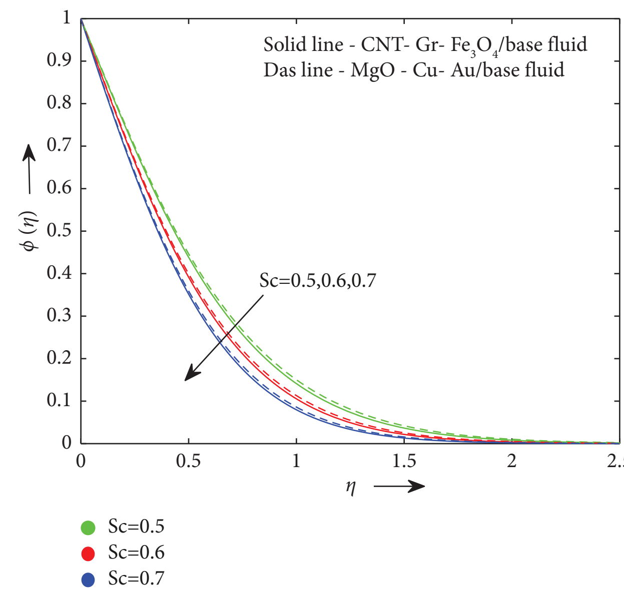

Figure 15: Concentration profile for Schmidt number Sc.

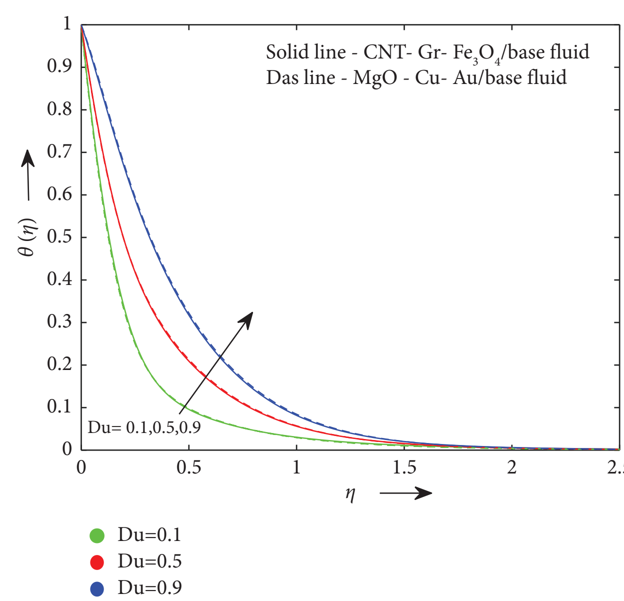

Figure 16: Temperature distribution for Dufour effect Du.

absorption Q. As the heat source/sink rises, the thermal boundary layer thickness enhances, causing the thermal to rise for ternary groups I and II.

It can be seen in Figures 19–22 that the motion distributions ($f'(\eta)$ and $g'(\eta)$), thermal distribution, and concentration level decrease with rising values of the stretching ratio parameter c for both the ternary groups. The physical features for the Figures 23–28 are as follows: $Pr = 21, \beta = 0.06$, $M = 8, f_w = 0.3$, $Nr = 1$, $Ec = 0.5$, $Kr = 0.5$, $\mathrm{Sc} = 0.7$, $c = 4$, $Du = 0.5$, $Sr = 0.1 = Q$ and $\phi_1 = \phi_2 = 0.15$, and $\phi_3 = 0.01$. Figures 23–26 show that the motions $f'(\eta)$ and $g'(\eta)$ increase upon increasing the volume fraction of Fe_3O_4 and MgO nanoparticles, respectively, because the thickness of the barrier layer increases. Figures 27 and 28 define the enhancement in $\theta(\eta)$ with amplifying the volume fraction of Fe_3O_4 and the volume fraction of MgO nanoparticles. It is related to the improvement in the nanofluids thermal conductivity that comes from the existence of larger nanoparticles.

Tables 4 and 5 express the rates of skin friction (x and y directions), heat transportation, and mass transport. When $\beta = 0.06$, $M = 6$, $f_w = 0.3$, $\mathrm{Nr} = 1$, $\mathrm{Kr} = \mathrm{Ec} = \mathrm{Du} = 0.5$, $\mathrm{Sc} = 0.7$, $Q = \mathrm{Sr} = 0.1$, $c = 4$, $\mathrm{Pr} = 21$, and $\phi_1 = \phi_2 = 0.15$, $\phi_3 = 0.01$ for

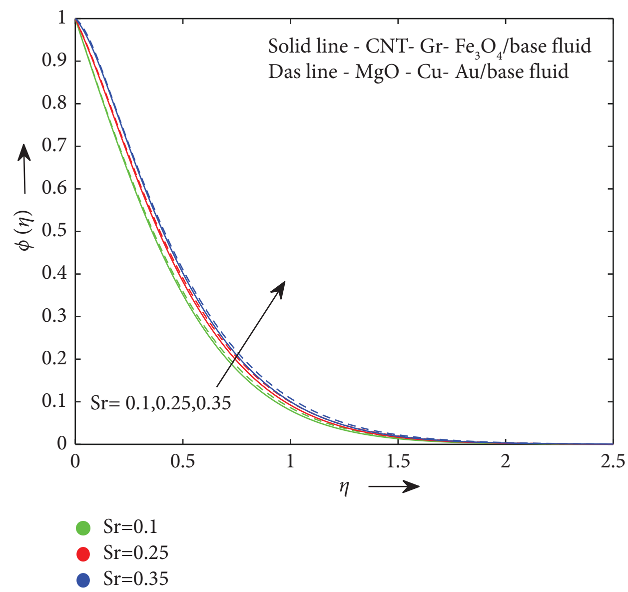

Figure 17: Concentration profile for Soret impact Sr.

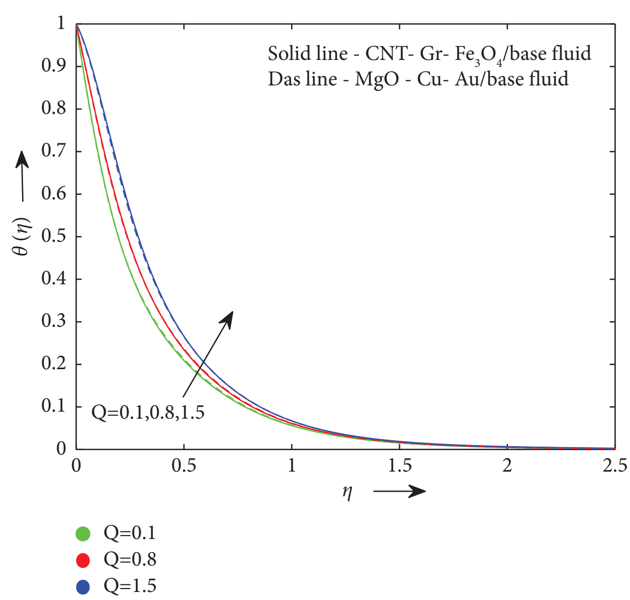

Figure 18: Temperature distribution for heat source/sink Q.

ternary groups I and II. Tables 3 and 4 portray the variation in Casson fluid parameter (β), magnetic impact (M), suction velocity (f_w), radiation parameter (Nr), Prandtl number (Pr), Eckert number (Ec), chemical reaction (Kr), Dufour impact (Du), Soret effect (Sr), stretching ratio parameter (c), Schmidt number (Sc), heat source/sink (Q) on heat flux coefficient, skin friction rate (in x and y directions), and mass transfer coefficient for ternary group I and ternary group II. When $\beta = 0.06$, $M = 8$, $f_w = 0.3$, $\mathrm{Nr} = 1$, $\mathrm{Kr} = \mathrm{Ec} = \mathrm{Du} = 0.5$, $\mathrm{Sc} = 0.7$, $Q = \mathrm{Sr} = 0.1$, $c = 4$, $\mathrm{Pr} = 21$, and $\phi_1 = \phi_2 = 0.15$, $\phi_3 = 0.01$ for both ternary groups, the skin friction rate in x and y directions are enhanced by the rising Casson fluid parameter, while the opposite impact is shown for the magnetic impact and suction velocity. The rate of heat transfer grows with rising radiation impact and Prandtl number, while the opposite effect is seen for Eckert number, Dufour impact, and heat source/sink. For both ternary groups, Sherwood number rises with enhancing Schmidt number, chemical reaction, and volume fraction of Fe_3O_4 and MgO. Furthermore, the Sherwood number decays when the Soret effect increases.

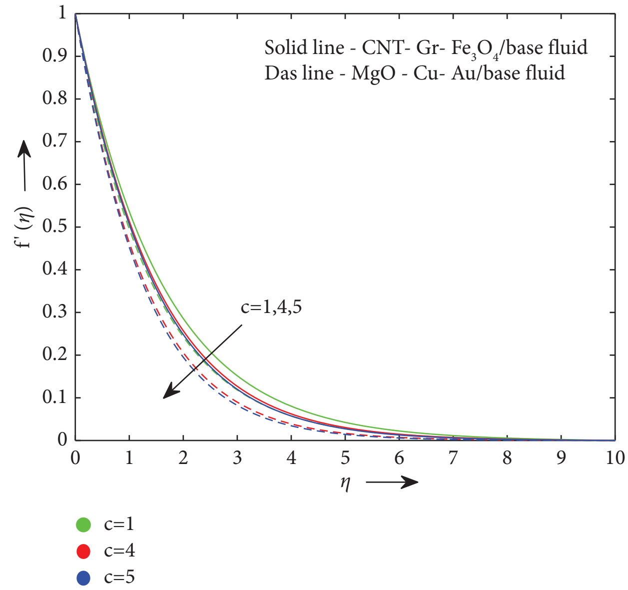

FIGURE 19: Velocity distribution $f'(\eta)$for stretching ratio parameter c.

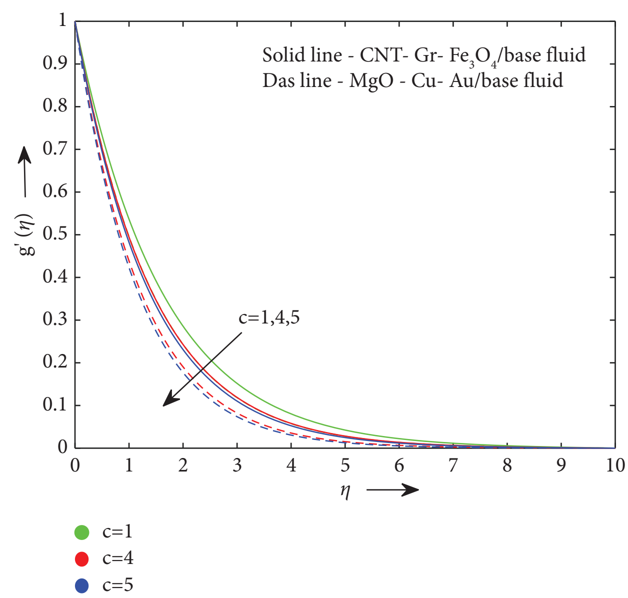

FIGURE 20: Velocity distribution $g'(\eta)$ for stretching ratio parameter c.

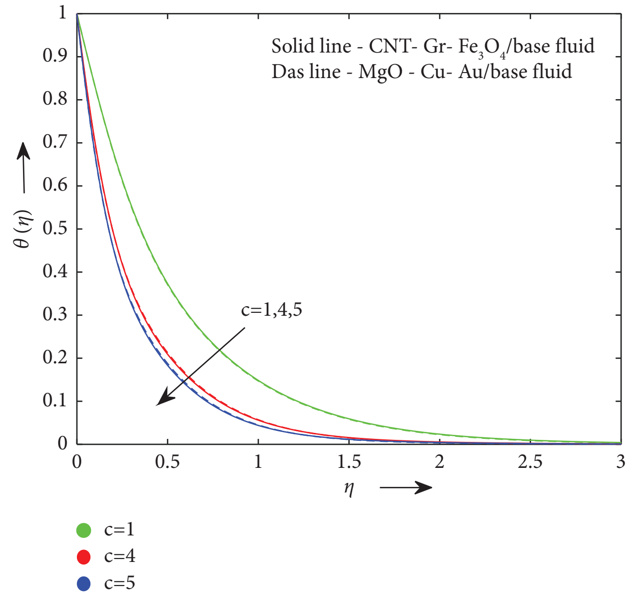

FIGURE 21: Temperature distribution for stretching ratio parameter c.

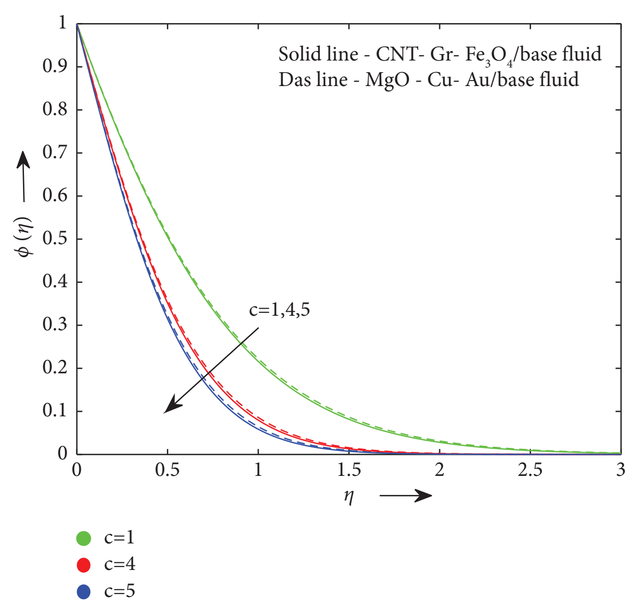

FIGURE 22: Concentration profile for stretching ratio parameter c.

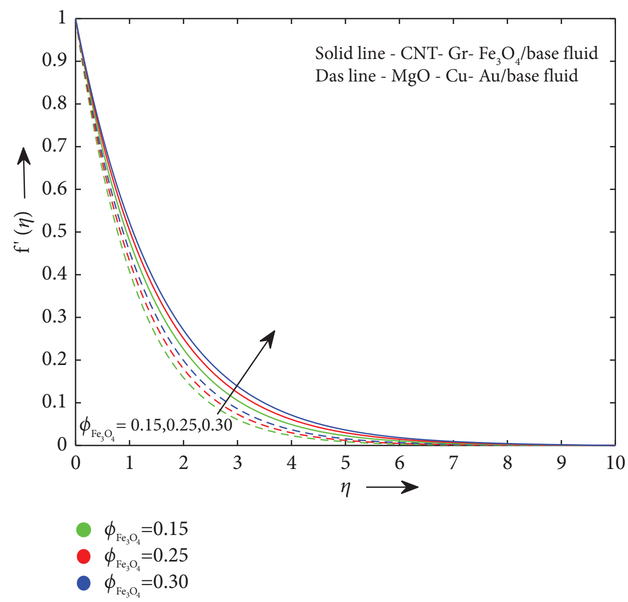

Figure 23: Velocity distribution in x direction for volume fraction of Fe_3O_4 $\phi_{Fe_3O_4}$.

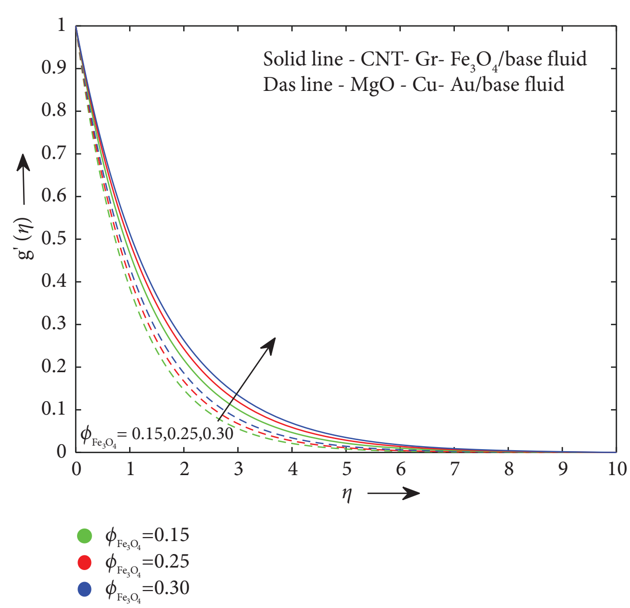

Figure 24: Velocity distribution in y direction for volume fraction of Fe_3O_4 $\phi_{Fe_3O_4}$.

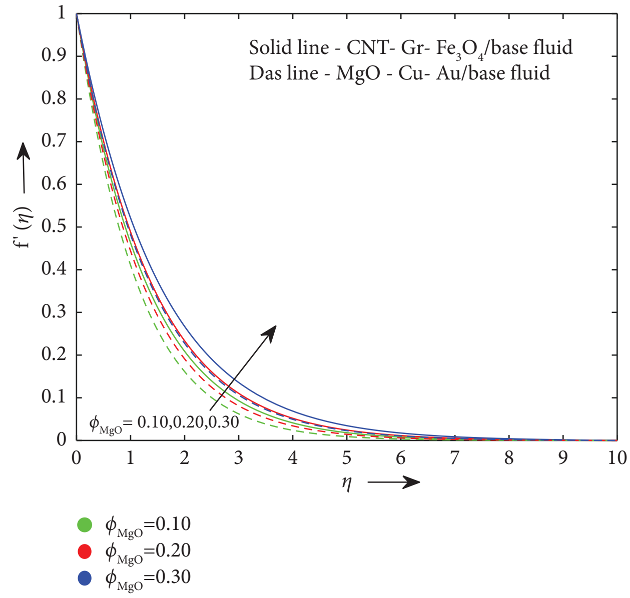

Figure 25: Velocity distribution $f'(\eta)$for volume fraction of MgO ϕ_{MgO}.

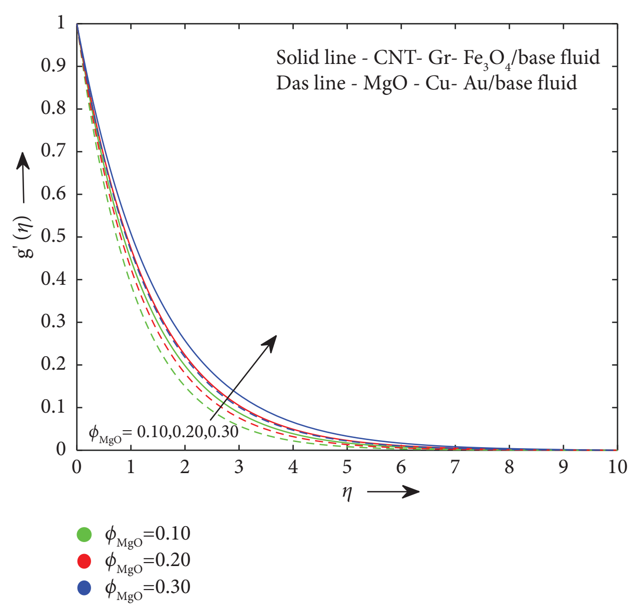

Figure 26: Velocity distribution $g'(\eta)$ for volume fraction of MgO ϕ_{MgO}.

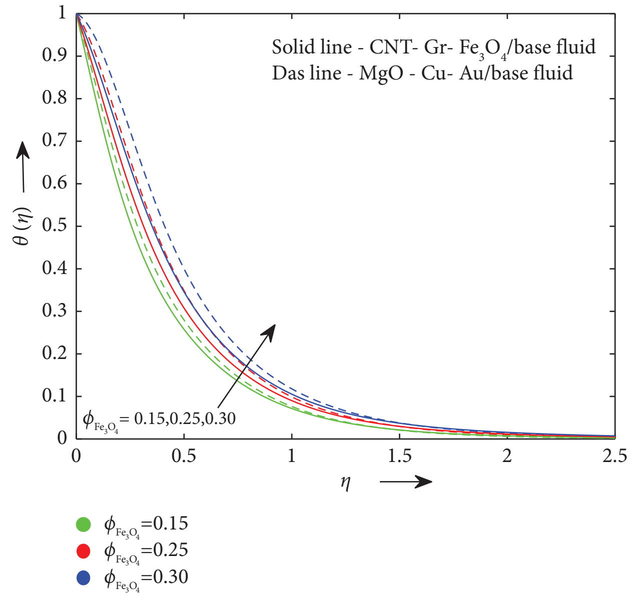

Figure 27: Temperature distribution for volume fraction of Fe_3O_4 $\phi_{Fe_3O_4}$.

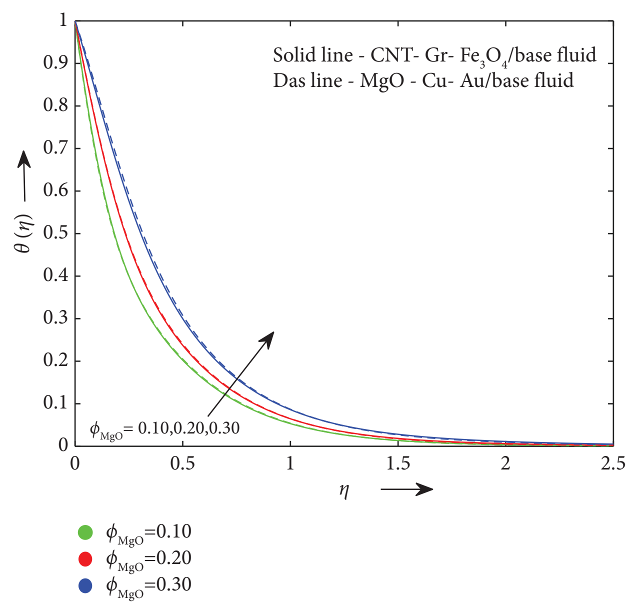

Figure 28: Temperature distribution for volume fraction of MgO ϕ_{MgO}.

Table 4: The rates of skin friction, Nusselt number and mass transfer with β, M, f_w and Nr when Kr = Ec = Du = 0.5, Sc = 0.7, Q = Sr = 0.1, c = 4, Pr = 21, and $\phi_1 = \phi_2 = 0.15$, $\phi_3 = 0.01$ for ternary groups I and II.

β	M	Q	Nr	Ternary group I				Ternary group II			
				$C_{f_x}\mathrm{Re}_x^{1/2}$	$C_{f_y}\mathrm{Re}_y^{1/2}$	$\mathrm{Nu}_x\mathrm{Re}_x^{-1/2}$	$\mathrm{Sh}_x\mathrm{Re}_x^{-1/2}$	$C_{f_x}\mathrm{Re}_x^{1/2}$	$C_{f_y}\mathrm{Re}_y^{1/2}$	$\mathrm{Nu}_x\mathrm{Re}_x^{-1/2}$	$\mathrm{Sh}_x\mathrm{Re}_x^{-1/2}$
0.04				−22.3390092	−24.1602647	10.9892558	1.5909429	−15.0275952	−16.6142091	11.0600046	1.5718261
0.05	6	0.1	1	−20.1071124	−21.7432540	11.1507114	1.5757060	−13.5377424	−14.9625194	11.2609060	1.5537863
0.06				−18.4681698	−19.9681808	11.2724315	1.5625263	−12.4434501	−13.7492891	11.4127341	1.5382075
	6			−18.4681698	−19.9681808	11.2724315	1.5625263	−12.4434501	−13.7492891	11.4127341	1.5382075
0.06	8			−20.7300381	−22.0759260	10.5012927	1.5639424	−13.8310922	−15.0156821	10.5749504	1.5409216
	10			−22.7665505	−23.9977513	9.7795854	1.5657461	−15.0903030	−16.1821333	9.78744231	1.5439017
		0.1		−18.4681698	−19.9681808	11.2724315	1.5625263	−12.4434501	−13.7492891	11.4127341	1.5382075
	6	0.8		−18.4681698	−19.9681808	7.59934540	2.1456425	−13.5545542	−14.8179213	7.69490730	1.6128870
		1.5		−18.4681698	−19.9681808	3.13385211	2.7869235	−14.7416146	−15.9588303	3.22487308	1.7025566
			1	−18.4681698	−19.9681808	11.2724315	1.5625263	−13.7492891	−13.7492891	11.4127341	1.5382075
		0.1	10	−18.4681698	−19.9681808	18.4850375	1.6360161	−13.7492891	−13.7492891	7.69490730	1.6613407
			20	−18.4681698	−19.9681808	24.2768514	1.7252113	−13.7492891	−13.7492891	3.22487308	1.6845646

Table 5: The rates of skin friction, Nusselt number and mass transfer with Sc, Kr, Du, and Sr when $\beta = 0.06$, $f_w = 0.3$, M = 6, Nr = 1, c = 4, Pr = 21, Ec = 0.5 and $\phi_1 = \phi_2 = 0.15$, and $\phi_3 = 0.01$ for ternary groups I and II.

Du	Sr	Sc	Kr	Ternary group I				Ternary group II			
				$C_{f_x}\mathrm{Re}_x^{1/2}$	$C_{f_y}\mathrm{Re}_y^{1/2}$	$\mathrm{Nu}_x\mathrm{Re}_x^{-1/2}$	$\mathrm{Sh}_x\mathrm{Re}_x^{-1/2}$	$C_{f_x}\mathrm{Re}_x^{1/2}$	$C_{f_y}\mathrm{Re}_y^{1/2}$	$\mathrm{Nu}_x\mathrm{Re}_x^{-1/2}$	$\mathrm{Sh}_x\mathrm{Re}_x^{-1/2}$
0.1				−18.4681698	−19.9681808	16.0175983	1.4716120	−12.4434501	−13.7492891	16.4893620	1.4404367
0.5	0.1	0.7	0.5	−18.4681698	−19.9681808	11.2724315	1.5625263	−12.4434501	−13.7492891	11.4127341	1.5382075
0.9				−18.4681698	−19.9681808	4.9645993	1.6855570	−12.4434501	−13.7492891	4.4244884	1.6753820
	0.1			−18.4681698	−19.9681808	11.2724315	1.5625263	−12.4434501	−13.7492891	11.4127341	1.5382075
0.5	0.25			−18.4681698	−19.9681808	14.3910003	1.1332189	−12.4434501	−13.7492891	15.1455224	1.0701425
	0.35			−18.4681698	−19.9681808	18.8027652	0.5709370	−12.4434501	−13.7492891	21.2874934	0.3638502
		0.5		−18.4681698	−19.9681808	12.9055087	1.2592024	−12.4434501	−13.7492891	13.1752533	1.2340872
	0.5	0.6		−18.4681698	−19.9681808	12.1001441	1.4132304	−12.4434501	−13.7492891	12.3088817	1.3882444
		0.7		−18.4681698	−19.9681808	11.2724315	1.5625263	−12.4434501	−13.7492891	11.4127341	1.5382075
			0.5	−18.4681698	−19.9681808	11.2724315	1.5625263	−12.4434501	−13.7492891	11.4127341	1.5382075
		0.7	2.5	−18.4681698	−19.9681808	8.1353632	2.0266751	−12.4434501	−13.7492891	7.91051453	2.0170952
			4.5	−18.4681698	−19.9681808	5.4255264	2.4178438	−12.4434501	−13.7492891	4.8998493	2.4181421

4. Conclusion

This innovative study clarifies the two groups of ternary nanoparticles (*CNT*-*Gr*-Fe_3O_4 and MgO-Cu-Au)/kerosene oil-based, 3D radiative MHD non-Newtonian Casson hybrid nanofluid flow across a dually stretch sheet with heat generation/absorption and viscous dissipation. Furthermore, the *BVP4c* solver was utilized during the solution procedure. The most essential results of our investigation are outlined as follows.

(i) When the Casson fluid parameter and magnetic effect are used in greater amounts, the fluid motion in the x and y directions are reduced for ternary group II than the ternary group I

(ii) The fluid temperature upsurges when enlarging the radiation parameter and heat generation/absorption for both ternary groups

(iii) The volume fraction of ternary nanoparticles boosts the motion (in both directions) and thermal distributions

(iv) A larger of Eckert number enhances the thermal profile, and there are no significant differences in the levels of the temperature distribution for both the ternary groups

(v) The Nusselt number enhances for both ternary group when rising thermal radiation

(vi) A larger value of Soret impact decays the mass transfer coefficient for ternary groups I and II

(vii) When compared to rising Dufour number (*Du*) and heat source/sink values, the Nusselt number depreciates

(viii) Sherwood number increases by increasing Schmidt number and chemical reaction

(ix) In the future, we can extend this work with different types of geometries, such as Riga plate and cylindrical surface, and different types of nanofluid cases

Nomenclature

u: X-axis velocity ($m \cdot s^{-1}$)
v: Y-axis velocity ($m \cdot s^{-1}$)
w: Z-axis velocity ($m \cdot s^{-1}$)
T: Fluid temperature (°C)
C: Fluid concentration (L^{-3})

T_w:	Solid wall temperature
C_w:	Solid wall concentration
T_∞:	Free stream temperature
C_∞:	Free stream temperature
B_0:	Magnetic field strength $(\mathrm{A\cdot m^{-1}})$
g:	Gravitational acceleration $(\mathrm{m\cdot s^{-2}})$
C_s:	Solid surface specific heat
Nu_x and Nu_y:	Nusselt number in x and y directions (dimensionless parameter)
τ_w:	Surface shear stress
q_w:	Heat transfer rate
Re_x and Re_y:	Reynolds number in x and y directions (dimensionless parameter)
C_{f_x} and C_{f_y}:	Skin friction in x and y directions (dimensionless parameter)
C_p:	Specific heat at constant pressure $(\mathrm{JK^{-1}\cdot kg^{-1}})$
hbnf:	Hybrid nanofluid
bf:	Base fluid
ϕ_1:	Volume fraction of first nanoparticle
ϕ_2:	Volume fraction of second nanoparticle
ϕ_3:	Volume fraction of third nanoparticle
K:	Thermal conductivity $(\mathrm{w\ m^{-1}\cdot K^{-1}})$
ρ:	Density $(\mathrm{kg\cdot m^{-3}})$
ν:	Kinematic viscosity $(\mathrm{m^2 s^{-1}})$
μ:	Dynamic viscosity $(\mathrm{kg\cdot m^{-1}\cdot s^{-1}})$
ρC_p:	Heat capacity $(\mathrm{J^0\cdot C^{-1}\cdot kg})$
μ_B:	Non-Newtonian fluid's plastic moveable viscosity
τ_y:	Yield stress for the fluid
z_w:	Suction rate
Q_0:	Heat source (>0)/sink (<0) amount
D_m:	Diffusivity
k_1:	Chemical reactive parameter
f_w:	Nondimensional suction parameter
q_r:	Flux of radiant heat
M:	Hartmann parameter/magnetic parameter
Pr:	Prandtl number
Ec:	Eckert number
Sc:	Schmidt number
Sr:	Soret number
Du:	Duffor number
Q:	Heat source/sink
C:	Ratio of stretching speed
Nr:	Radiation parameter
Kr:	Chemical reaction
η:	Pseudo-similarity variable
$f(\eta)$:	Nondimensional velocity of the motion in x-direction
$g(\eta)$:	Nondimensional velocity of the motion in y-direction
θ:	Nondimensional temperature parameter
φ:	Nondimensional concentration parameter.

Data Availability

The data used to support the findings of this study are available from the corresponding author upon request.

Conflicts of Interest

The authors declare that they have no conflicts of interest.

Authors' Contributions

All authors listed have made a substantial, direct, and intellectual contribution to the work and approved it for publication.

Acknowledgments

The study was supported by the Princess Nourah Bint Abdulrahman University Researchers Supporting Project number (PNURSP2023R59), Princess Nourah Bint Abdulrahman University, Riyadh, Saudi Arabia.

References

[1] F. Ahmad, S. Abdal, H. Ayed, S. Hussain, S. Salim, and A. O. Almatroud, "The improved thermal efficiency of Maxwell hybrid nanofluid comprising of graphene oxide plus silver/kerosene oil over stretching sheet," *Case Studies in Thermal Engineering*, vol. 27, Article ID 101257, 2021.

[2] T. Anwar, T. Anwar, P. Kumam, and S. Muhammad, "New fractional model to analyze impacts of Newtonian heating, shape factor and ramped flow function on MgO–SiO2–Kerosene oil hybrid nanofluid," *Case Studies in Thermal Engineering*, vol. 38, Article ID 102361, 2022.

[3] S. Bilal, M. I. Asjad, S. U. Haq, M. Y. Almusawa, E. M. Tag-ElDin, and F. Ali, "Significance of Dufour and Soret aspects on dynamics of water based ternary hybrid nanofluid flow in a 3D computational domain," *Scientific Reports*, vol. 13, no. 1, p. 4190, 2023.

[4] T. Elnaqeeb, I. L. Animasaun, and N. A. Shah, "Ternary-hybrid nanofluids: significance of suction and dual-stretching on three-dimensional flow of water conveying nanoparticles with various shapes and densities," *Zeitschrift für Naturforschung A*, vol. 76, no. 3, pp. 231–243, 2021.

[5] S. O. Giwa, M. Sharifpur, J. P. Meyer, S. Wongwises, and O. Mahian, "Experimental measurement of viscosity and electrical conductivity of water-based γ-Al 2 O 3/MWCNT hybrid nanofluids with various particle mass ratios," *Journal of Thermal Analysis and Calorimetry*, vol. 143, pp. 1037–1050, 2021.

[6] G. Huminic and A. Huminic, "The heat transfer performances and entropy generation analysis of hybrid nanofluids in a flattened tube," *International Journal of Heat and Mass Transfer*, vol. 119, pp. 813–827, 2018.

[7] S. Jakeer, S. R. R. Reddy, A. M. Rashad, M. Lakshmi Rupa, and C. Manjula, "Nonlinear analysis of Darcy-Forchheimer flow in EMHD ternary hybrid nanofluid (Cu-CNT-Ti/water) with radiation effect," *Forces in Mechanics*, vol. 10, Article ID 100177, 2023.

[8] M. V. Krishna, "Chemical reaction, heat absorption and Newtonian heating on MHD free convective Casson hybrid nanofluids past an infinite oscillating vertical porous plate," *International Communications in Heat and Mass Transfer*, vol. 138, Article ID 106327, 2022.

[9] A. Majeed, N. Golsanami, B. Gong et al., "Analysis of thermal radiation in magneto-hydrodynamic motile gyrotactic micro-organisms flow comprising tiny nanoparticle towards

a nonlinear surface with velocity slip," *Alexandria Engineering Journal*, vol. 66, pp. 543–553, 2023.

[10] S. M. Mousavi, M. N. Rostami, M. Yousefi, S. Dinarvand, I. Pop, and M. A. Sheremet, "Dual solutions for Casson hybrid nanofluid flow due to a stretching/shrinking sheet: a new combination of theoretical and experimental models," *Chinese Journal of Physics*, vol. 71, pp. 574–588, 2021.

[11] G. Mahanta and S. Shaw, "3D Casson fluid flow past a porous linearly stretching sheet with convective boundary condition," *Alexandria Engineering Journal*, vol. 54, no. 3, pp. 653–659, 2015.

[12] G. Mandal and D. Pal, "Estimation of entropy generation and heat transfer of magneto hydrodynamic quadratic radiative Darcy–Forchheimer cross hybrid nanofluid (GO+ Ag/kerosene oil) over a stretching sheet," *Numerical Heat Transfer, Part A: Applications*, vol. 84, no. 8, pp. 853–876, 2023.

[13] M. K. Nayak, G. Mahanta, M. Das, and S. Shaw, "Entropy analysis of a 3D nonlinear radiative hybrid nanofluid flow between two parallel stretching permeable sheets with slip velocities," *International Journal of Ambient Energy*, vol. 43, no. 1, pp. 8710–8721, 2022.

[14] S. Nasir, S. Sirisubtawee, P. Juntharee, A. S. Berrouk, S. Mukhtar, and T. Gul, "Heat transport study of ternary hybrid nanofluid flow under magnetic dipole together with nonlinear thermal radiation," *Applied Nanoscience*, vol. 12, no. 9, pp. 2777–2788, 2022.

[15] M. B. Patil, K. C. Shobha, S. Bhattacharyya, and Z. Said, "Soret and Dufour effects in the flow of Casson nanofluid in a vertical channel with thermal radiation: entropy analysis," *Journal of Thermal Analysis and Calorimetry*, vol. 148, no. 7, pp. 2857–2867, 2023.

[16] S. Kumar Rawat, M. Yaseen, U. Khan et al., "Insight into the significance of nanoparticle aggregation and non-uniform heat source/sink on titania–ethylene glycol nanofluid flow over a wedge," *Arabian Journal of Chemistry*, vol. 16, no. 7, Article ID 104809, 2023.

[17] M. Ramzan, A. Dawar, A. Saeed, P. Kumam, K. Sitthithakerngkiet, and S. A. Lone, "Analysis of the partially ionized kerosene oil-based ternary nanofluid flow over a convectively heated rotating surface," *Open Physics*, vol. 20, no. 1, pp. 507–525, 2022.

[18] G. Revathi, S. Avadapu, C. S. K. Raju et al., "Dynamics of lorentz force and cross-diffusion effects on ethylene glycol-based hybrid nanofluid flow amidst two parallel plates with variable electrical conductivity: a multiple linear regression analysis," *Case Studies in Thermal Engineering*, vol. 41, Article ID 102603, 2023.

[19] P. S. Reddy, P. Sreedevi, and S. Venkateswarlu, "Impact of modified Fourier's heat flux on the heat transfer of MgO/Fe3O4–Eg-based hybrid nanofluid flow inside a square chamber," *Waves in Random and Complex Media*, pp. 1–23, 2022.

[20] S. P. Singh, M. Kumar, M. Yaseen, and S. K. Rawat, "Ternary hybrid nanofluid (TiO2–SiO2–MoS2/kerosene oil) flow over a rotating disk with quadratic thermal radiation and Cattaneo-Christov model," *Journal of Central South University*, vol. 30, no. 4, pp. 1262–1278, 2023.

[21] N. Shaheen, M. Ramzan, A. Alshehri, Z. Shah, and P. Kumam, "Soret–Dufour impact on a three-dimensional Casson nanofluid flow with dust particles and variable characteristics in a permeable media," *Scientific Reports*, vol. 11, no. 1, Article ID 14513, 2021.

[22] H. M. Sayed and H. A. Hosham, "Dynamics and bifurcations of non-Newtonian Au–Cu/blood hybrid nanofluid model of electrokinetic flow in asymmetrically tapered wave microchannel," *Waves in Random and Complex Media*, pp. 1–18, 2022.

[23] K. Sarada, F. Gamaoun, A. Abdulrahman et al., "Impact of exponential form of internal heat generation on water-based ternary hybrid nanofluid flow by capitalizing non-Fourier heat flux model," *Case Studies in Thermal Engineering*, vol. 38, Article ID 102332, 2022.

[24] N. Sandeep, B. Ranjana, S. P. Samrat, and G. P. Ashwinkumar, "Impact of nonlinear radiation on magnetohydrodynamic flow of hybrid nanofluid with heat source effect," *Proceedings of the Institution of Mechanical Engineers- Part E: Journal of Process Mechanical Engineering*, vol. 236, no. 4, pp. 1616–1627, 2022.

[25] T. Gupta, A. K. Pandey, and M. Kumar, "Numerical study for temperature-dependent viscosity based unsteady flow of GP-MoS2/C2H6O2-H2O over a porous stretching sheet," *Numerical Heat Transfer, Part A: Applications*, pp. 1–22, 2023.

[26] H. Upreti, A. K. Pandey, Z. Uddin, and M. Kumar, "Thermophoresis and Brownian motion effects on 3D flow of Casson nanofluid consisting microorganisms over a Riga plate using PSO: a numerical study," *Chinese Journal of Physics*, vol. 78, pp. 234–270, 2022.

[27] A. Ullah, R. A. ZeinEldin, and H. A. E. W. Khalifa, "Investigation of the three-dimensional hybrid casson nanofluid flow: a cattaneo–christov theory," *ACS omega*, vol. 8, 2023.

[28] I. Zari, A. Shafiq, T. S. Khan, and S. Haq, "Marangoni convective flow of GO-kerosene-and GO-water-based casson-nanoliquid toward a penetrable riga surface," *Brazilian Journal of Physics*, vol. 51, no. 6, pp. 1747–1762, 2021.

[29] Q. Zaigham Zia, I. Ullah, M. A. Waqas, A. Alsaedi, and T. Hayat, "Cross diffusion and exponential space dependent heat source impacts in radiated three-dimensional (3D) flow of Casson fluid by heated surface," *Results in Physics*, vol. 8, pp. 1275–1282, 2018.

[30] W. Ahmed, S. N. Kazi, Z. Z. Chowdhury et al., "Heat transfer growth of sonochemically synthesized novel mixed metal oxide ZnO+ Al2O3+ TiO2/DW based ternary hybrid nanofluids in a square flow conduit," *Renewable and Sustainable Energy Reviews*, vol. 145, Article ID 111025, 2021.

[31] S. M. Mousavi, F. Esmaeilzadeh, and X. P. Wang, "Effects of temperature and particles volume concentration on the thermophysical properties and the rheological behavior of CuO/MgO/TiO 2 aqueous ternary hybrid nanofluid: experimental investigation," *Journal of Thermal Analysis and Calorimetry*, vol. 137, no. 3, pp. 879–901, 2019.

[32] S. Dolui, B. Bhaumik, and S. De, "Combined effect of induced magnetic field and thermal radiation on ternary hybrid nanofluid flow through an inclined catheterized artery with multiple stenosis," *Chemical Physics Letters*, vol. 811, Article ID 140209, 2023.

[33] S. Nasir, S. Sirisubtawee, T. Gul, P. Juntharee, W. Alghamdi, and I. Ali, "Thermal characteristics of nonlinear convection and radiation for the flow of tri-hybrid nanofluids over stretchable surface with energy source," *Surface Review and Letters*, vol. 29, no. 11, Article ID 2250153, 2022.